ORIGINAL ARTICLE

Underground hyperspectral outcrop scanning for automated mine-face mapping: The lithium deposit of Zinnwald/Cínovec

Moritz Kirsch[1] | **Maria Mavroudi[1,2]** | **Sam Thiele[1]** | **Sandra Lorenz[1]** | **Laura Tusa[3]** | **René Booysen[1,4]** | **Erik Herrmann[1]** | **Ayoub Fatihi[1,5]** | **Robert Möckel[1]** | **Thomas Dittrich[6]** | **Richard Gloaguen[1]**

[1]Helmholtz-Zentrum Dresden-Rossendorf, Helmholtz Institute Freiberg for Resource Technology, Freiberg, Germany

[2]School of Mining and Metallurgical Engineering, National Technical University of Athens, Athens, Greece

[3]TheiaX GmbH, Freiberg, Germany

[4]School of Geosciences, University of the Witwatersrand, Johannesburg, South Africa

[5]IAV Hassan II, School of Geomatics and Surveying Engineering, Rabat, Morocco

[6]Deutsche Lithium GmbH, Freiberg, Germany

Correspondence
Moritz Kirsch, Helmholtz-Zentrum Dresden-Rossendorf, Helmholtz Institute Freiberg for Resource Technology, Freiberg, Germany.
Email: m.kirsch@hzdr.de

Abstract

The inherent complexity of underground mining requires highly selective ore extraction and adaptive mine planning. Repeated geological face mapping and reinterpretation throughout mine life is therefore routine in underground mines. Hyperspectral imaging (HSI) has successfully been applied to enhance geological mapping in surface mining environments, but remains a largely unexplored opportunity in underground operations due to challenges associated with illumination, wet surfaces and data corrections. In this study, we propose a workflow that paves the way for the operational use of HSI in active underground mines. In a laboratory set-up, we evaluated different hyperspectral sensors and lighting set-ups as well as the effect of surface moisture. We then acquired hyperspectral data in an underground mine of the Zinnwald/Cínovec Sn-W-Li greisen-type deposit in Germany. These data were corrected for illumination effects, back-projected into three dimensions and then used to map mineral abundance and estimate Li content across the mine face. We validated the results with handheld laser-induced breakdown spectroscopy. Despite

remaining challenges, we hope this study will help establish hyperspectral sensors in the extractive industry as a means to increase the volume and efficiency of raw material supply, advance digitalisation, and reduce the environmental footprint and other risks associated with underground mining.

KEYWORDS
hyperspectral, lithium, mineral mapping, point cloud, underground mining

INTRODUCTION

Outcrop mapping provides crucial geological information in the exploration, evaluation and mining phases of mineral resource development. It is also an essential part of quality and process control and geotechnical risk assessments. Hence, decisions made on the basis of geological mapping at the extraction sites have direct implications for mine profitability, safety and environmental impact (e.g., Panagiotou & Michalakopoulos, 2020). Traditionally, geologists visually conduct geological mapping in mines, that is, in direct contact with the outcrop. This method is time-consuming, inefficient and subjective, and can be dangerous as recently blasted outcrops are potentially unstable and prone to rockfall. For this reason, various methods have been developed for remote mapping of mine walls, focusing on two types of data: (1) detailed three-dimensional (3D) outcrop models (e.g., Rossi et al., 2017; Tong et al., 2015) and (2) two-dimensional (2D) hyperspectral images from which information on material composition can be derived (e.g., Fraser et al., 2006; Hunt, 1977; Murphy & Monteiro, 2013; Yang et al., 2013). Recent studies have merged high-resolution point clouds with hyperspectral images into *hyperclouds* (Kirsch et al., 2018, 2019; Kurz et al., 2011; Lorenz et al., 2018; Taylor et al., 2013; Thiele et al., 2021). These datasets have significant potential for the mining industry as they allow for the integrated representation, analysis, and interpretation of geometric and spectral features. As recently shown in several studies, the *hypercloud* approach can effectively support exploration and mining activities (e.g., Booysen et al., 2022; Guarnieri et al., 2022; Kirsch et al., 2018; Lorenz et al., 2018; Murphy et al., 2015; Thiele et al., 2021).

Although hyperspectral imaging (HSI) has been proven to add value to exploration activities in surface mining environments, it has yet to be fully demonstrated in underground settings. The development of these techniques for underground mining is of high relevance for two main reasons: (1) compared with open-pit mining, in which both low- and high-grade zones of the ore body are typically mined, a more selective mining strategy is favoured in underground mining (Nassar et al., 2022; Nwaila et al., 2022), making the identification of ore versus gangue through geological face mapping critically important; and (2) currently, about 40% of worldwide mining operations are underground (Martino et al., 2021), a number expected to rise over the coming years due to the increasing depth of remaining mineral deposits and as part of the effort to reduce the environmental and societal footprint of mining (e.g., Sahu et al., 2015). However, underground mining operations are comparatively expensive and low volume, accounting for only 12% of global run-of-mine productions (Martino et al., 2021). Despite, and to some extent, because of the inherent complexities of underground mining, there are many opportunities for improving its productivity, for instance, through increased digitalisation and automation (Ghamisi et al., 2021; Lööw et al., 2019; Nwaila et al., 2022).

Underground environments present a challenge for hyperspectral outcrop analysis because of poor illumination, air and surface moisture, and limited accessibility. Only a few studies have explored hyperspectral data acquisition in underground environments. Kurz et al. (2017) used a HySpex SWIR-320m (1.3–2.5 μm) hyperspectral sensor positioned at different distances to map mineralogy in an underground rock laboratory using halogen light sources. Lobo et al. (2021) scanned hand samples with a Specim FX17 (0.9–1.7 μm) hyperspectral camera in a dark

lab set-up with artificial illumination simulating gallery mine conditions and then evaluated machine-learning methods to identify and map the mineral distribution. However, to date, there has not been a systematic investigation of the effect of light, moisture and equipment on the spectral quality and geological interpretation, and the feasibility of applying hyperspectral methods under real underground conditions remains largely unknown. To address this gap in knowledge, our contribution includes a laboratory study to evaluate different light/sensor set-ups and the effect of surface moisture. Based on results of the lab study, a field study in an underground mine showcases adapted workflows for the acquisition and correction of underground hyperspectral scans using the *hypercloud* approach. We then use a novel workflow for combining sample mineralogy from quantitative X-ray diffraction (XRD) measurements and hyperspectral unmixing techniques to derive quantitative mineral abundance maps. We also demonstrate the application of handheld laser-induced breakdown spectroscopy (LIBS) for efficient external validation of mineral maps. As a case study, we chose the Zinnwald underground mine in Erzgebirge, Germany, where rocks of the Zinnwald/Cínovec Sn-W-Li greisen-type deposit are exposed, because (1) the ore, Li, has a strategic relevance for many developed countries (Azevedo et al., 2022; European Commission, 2020); (2) easy access is warranted as it has a visitor section; and (3) the lighting and humidity conditions in the mine are representative of many underground mines. Despite some remaining challenges, our results are promising and confirm the feasibility of hyperspectral methods for (automated) outcrop mapping in real underground mining operations.

GEOLOGICAL SETTING

The Zinnwald/Cínovec greisen-type ore deposit, located in the Eastern Erzgebirge/Krušné hory, about 3 km south of Altenberg along the German–Czech border (Figure 1A), is one of the most important Sn-W deposits of the Central European Variscides. It has been mined for Sn and W for several centuries (Neßler, 2016, *passim*) and has recently gained economic significance for its Li resources (Dittrich et al., 2020; Neßler, 2016). Most of the Li mineralisation is contained in zinnwaldite, a Li-Fe mica (average Li content of 1.7 wt%; Neßler, 2016) mainly occurring in horizontal to gently dipping, subparallel greisen bodies within the uppermost 100 m of the Late Variscan Zinnwald granite intrusion (Figure 1B) (Tischendorf & Forster, 1990). The Zinnwald granite belongs to the Altenberg-Teplice-Caldera (Stemprok et al., 2003; Tomek et al., 2021), which is associated with (but postdates) the extrusion of voluminous dacitic to rhyolitic lavas as well as the emplacement of multiphase granitic and microgranitic intrusions at about 325–312 Ma. Using brittle structures within the cooling granite as pathways, metal-bearing hydrothermal fluids then partially greisenised the granite (Neßler, 2016).

The three outcrops of the case study are located in an 8–12 m wide, 25 m long and up to 2 m high widening in the north-western portion of "Flöz 8", accessible through the Tiefer Bünau adit of the Zinnwald visitor's mine (Figure 1C). The granite exposed in this location exhibits different degrees of greisenisation as well as clay and haematite alteration. Whereas the unaltered albite granite (not exposed in these outcrops) is composed of quartz, plagioclase, orthoclase and muscovite, the greisen contains mostly quartz and zinnwaldite, with minor muscovite, K-feldspar, topaz, kaolinite and fluorite (Neßler, 2016). A few sub-horizontal 10–20 cm-thick quartz-muscovite veins ("Flözgänge") lined with nests of zinnwaldite and topaz intersect the outcrops, locally offset by small subvertical faults.

METHODS

Sampling

We collected 10 large (>20 cm diameter) hand samples of representative lithologies at Zinnwald mine for a feasibility lab study. At the Georgenfelder Querschlag (Figure 1C), rhyolite, albite granite with haematite-alteration (granite-A), sericite-alteration (granite-B, C) and kaolinite-alteration (granite-D) were sampled (Figure 2A). Greisen samples,
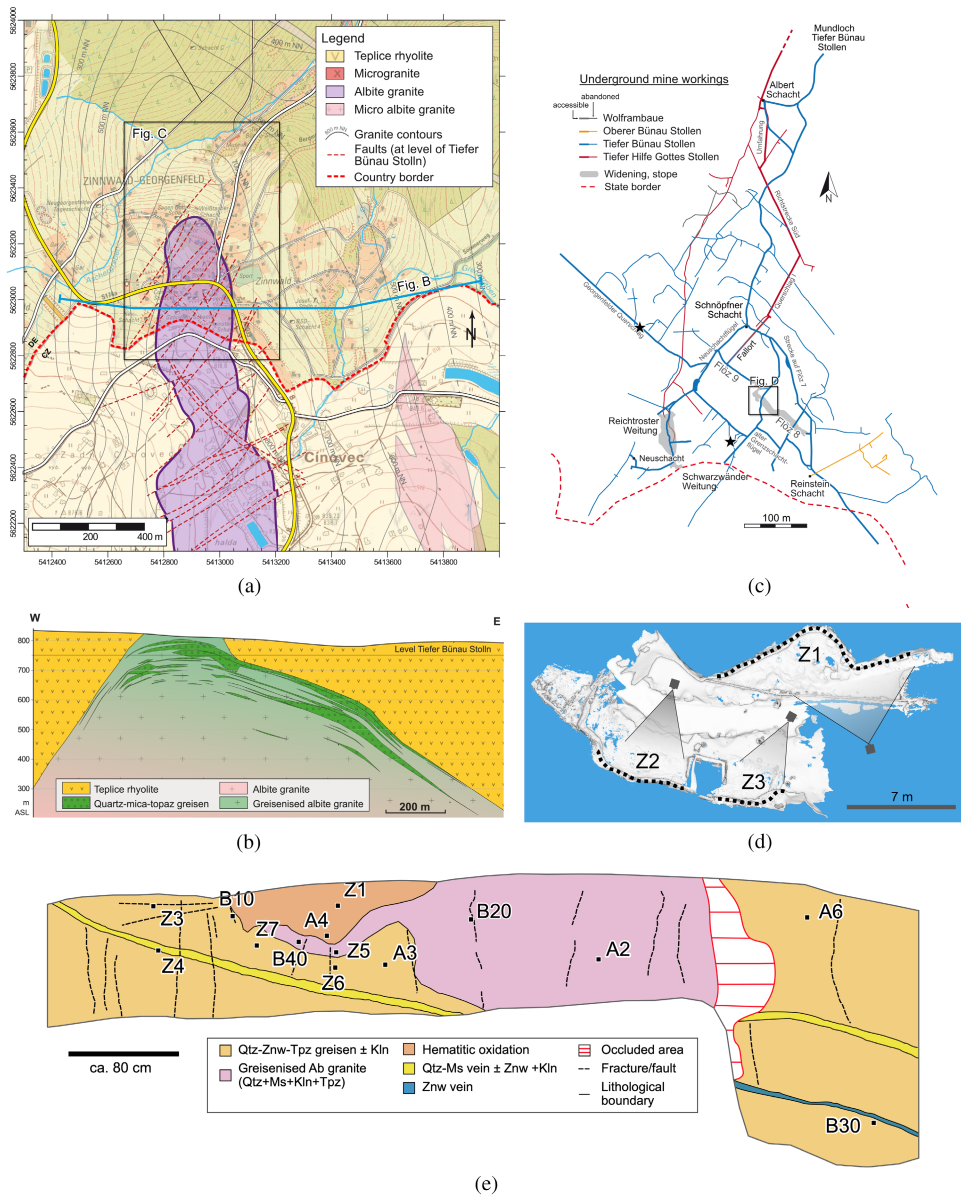
FIGURE 1 (a) Geological map; (b) cross-section of the study area with sample locations shown as black stars. (c) Underground drifts in the Zinnwald area showing scanning locations; and (d) in Flöz 9. (e) Field sketch of outcrop Z1 including sample locations. (a–c) Modified after Neßler (2016); base map in (a) GeoSN (2013); mineral abbreviation in (e) after Whitney and Evans (2010).

including a quartz greisen (greisen-A) a kaolinite-rich greisen (greisen-B), a haematite-rich greisen (greisen-C), a quartz–mica greisen (greisen-D) and a quartz-zinnwaldite-topaz greisen (greisen E), were collected at the Grenzschachtflügel (Figure 1C). The samples were cleaned and subsequently mounted rigidly on wooden boards with metal wires to enable the co-registration of the corresponding hyperspectral data cubes acquired in different scanning set-ups.

In addition, we collected 14 samples from outcrop Z1 for quantitative mineral abundance measurements using XRD (Figure 1E; and see the "Mineral mapping and estimation" section). Sample selection was based on field observations and hyperspectral data to ensure that these captured the main mineralogical variability of the outcrop.

Laboratory tests

Drillcore scanner

We acquired reference hyperspectral data of all hand samples using a Specim SisuRock Scanner equipped with a push-broom Specim AisaFenix hyperspectral sensor (Figure 1B; sensor specifications are described in Table 1). For data acquisition, the sample boards were placed on a tray moving below the line sensor (sensor–target distance about 1 m) to build a spectral data cube. The scanning line is evenly illuminated during the measurement with two arrays of quartz–halogen lights (each with ten 35 W bulbs). A spectral reference target (Spectralon SRS-99 reflectance standard) covering the entire width of the tray is acquired during each measurement for radiance-to-reflectance conversion and compensation of across-track illumination effects.

Dark lab set-up

To simulate underground scanning conditions in a lab, we used a dark room with complete sealing from ambient light (Figure 2C). The prepared sample boards were mounted vertically on one wall of the room. Sensors and light sources to be tested were set up on a tripod, facing the wall obliquely. We placed a spectral reference target (Zenith Light, 95% reflectance, 100 × 100 cm) in the scene with the same orientation and distance to the sensors.

The dark lab set-up had three objectives: (1) test and compare different light sources and set-ups (distance, focus, combination of light sources); (2) test and compare different visible–near-infrared (VNIR)–short-wave infrared range (SWIR) hyperspectral camera systems in simulated underground conditions; and (3) investigate the influence of moist and wet surface conditions on the measurements.

For the light tests, we included four different light sources: a heat lamp and three quartz–halogen lamps, that is, a floodlight, a spotlight and a film lamp, with different power and focus options (Table 2). Light-emitting diodes (LEDs) were not considered in these experiments because they emit light in discrete, narrow excitation peaks (e.g., Elvidge et al., 2010), and currently, commercial LEDs only cover the visible to SWIR up to about 1750 nm. The lights were set up on a tripod at varying distances (1.5–4 m) from a Spectralon white panel, and the radiance of the reflected light was measured using a portable Spectral Evolution PSR 3500 spectroradiometer (Spectral Evolution) with a 1° fibre mount lens.

The sensor tests included a SPECIM AisaFenix, a SPECIM AisaFenix 1K and a HySpex Mjølnir VS-620 (for the detailed sensor specifications, see Table 1). We set up all sensors in the same spot and orientation, at about a 5 m distance from the mounted samples (Figure 2C). For illumination, three halogen lamps (floodlight, spotlight and film lamp) were placed around the target at about 2–2.5 m distance.

To investigate the effect of moisture on the measurements, additional scans were performed with the Fenix 1K set-up and a combination of three halogen lamps (floodlight, spotlight and film lamp). After measuring the dry rock surface, the samples were evenly wetted with a water sprayer to simulate a moist environment. For a wet surface measurement, the samples were sprayed until saturation, indicated by excess water run-off.

Data processing and co-registration

The Fenix and Fenix 1K raw data were converted to radiance using the open-source hyperspectral processing toolbox *hylite* (Thiele et al., 2021) to perform dark current subtraction, bad pixel removal and apply sensor-specific gain and offset values. For the Mjølnir data, we performed this step using the HySpexRad software (version 2.5), including additional corrections for the sensor-specific smile and keystone effects.
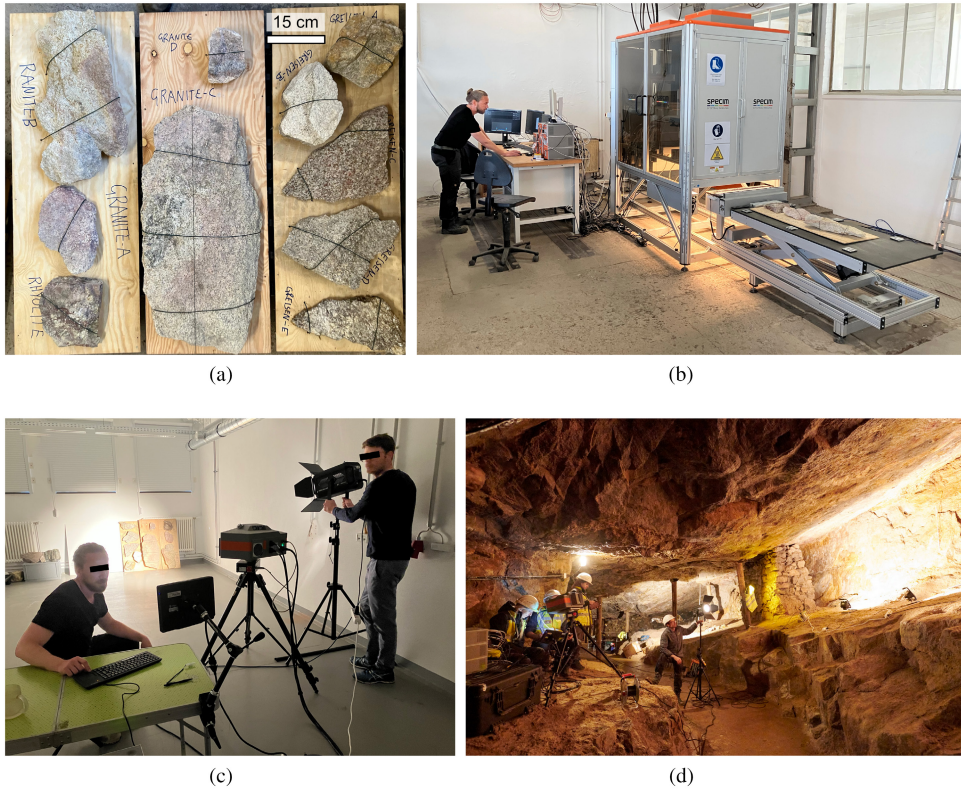
FIGURE 2 (a) Sample board with hand specimens of rocks from Zinnwald mine; (b) SisuRock drill core scanner set-up; (c) dark lab set-up for lighting, sensor and moisture tests; and (d) acquisition set-up in the underground mine.

The radiance data were further processed using *hylite* (1) to convert to reflectance using calibration panel spectra and the empirical line correction method; (2) to apply geometric corrections to remove lens distortions; (3) to co-register the data from different sensors using manually selected image tie points; and (4) to perform minimum wavelength mapping and false colour visualisations.

Underground mapping application

Geometric data

To generate digital outcrop models of the imaged scenes, we first scanned the outcrops with the built-in LiDAR sensor of an iPhone 12 Pro by walking along the rock faces at a <5 m distance. We chose this approach to demonstrate the added value of accessible, consumer-grade technology and highlight its potential in future mobile solutions for hypercloud generation. The iPhone 12 Pro features a Vertical Cavity Surface Emitting Laser (VCSEL) in a near-infrared spectrum and yields a point density of 7225 points m^{-2} at 25 cm distance and 150 points m^{-2} at 250 cm distance (Luetzenburg et al., 2021).

To achieve higher spatial resolution across the scanned areas, we additionally captured 329 high-resolution (8256 × 5504 pixels) RGB images from multiple viewpoints around the outcrops using a Nikon D850 DSLR camera with a Nikon AFS Nikkor 35 mm f/1.8G ED lens. To attain an even illumination in the RGB texture of the resulting model, we used a Nikon SB-700 AF Speedlight on-camera flash unit with no additional external

TABLE 1 Hyperspectral sensors used in this study.

	SPECIM AisaFenix	SPECIM AisaFenix 1K	HySpex Mjølnir VS-620
Spectral range (nm)	380–2500	380–2500	400–2500
Bands (spectral binning)	VNIR: 175 (4)	VNIR: 348 (2)	VNIR: 200 (–)
	SWIR: 275 (–)	SWIR: 256 (–)	SWIR: 300 (–)
	Combined: 450	Combined: 604	Combined: 490
Spatial resolution (pixels)	Combined: 384	Combined: 1024	VNIR: 1240
			SWIR: 620
			Combined: 620
Ground sampling distance (GSD) (cm/pixel) at 7 m distance	1.3	0.5	0.4
Field of view (°)	32.3	40	20
Spectral resolution (FWHM)	VNIR 3.5	VNIR 4.5	VNIR 3.0–3.6
	SWIR 12	SWIR 14	SWIR 5.1–5.6
Spectral sampling	VINR 3.4	VNIR 1.7	VNIR 3.0
	SWIR 5.7	SWIR 6.3	SWIR 5.1
Peak signal-to-noise ratio (SNR)	VNIR 600–1000:1	VNIR 600–1000:1	VNIR 180:1
	SWIR 1050:1	SWIR 1250:1	SWIR 900:1
Weight (kg)	15.0	22.5	6
Sensor type	Push-broom	Push-broom	Push-broom
Dimensions (l–w–h)	450–387–223 mm	530–530–210 mm	374–202–178 mm
Maximum power consumption (W)	500	300	50 (battery-powered)
Focus distance (m)	Adjustable (1–∞)	∞ (>10)	∞ (>20–25)
Approximate relative cost	1.3	3.7	1

Abbreviations: FWHM, full width at half maximum; SWIR, short-wave infrared; VNIR, visible–near-infrared.

TABLE 2 Light sources tested in this study.

Light type	Power (W)	Approximate field of view (°)	Approximate irradiance at 4.5 m distance (W/m^2)
Halogen floodlight	500	30	354
Halogen film lamp	1000	60	153
Halogen spotlight	1000	12–53	4610–205
Heat lamp (STIR® Infrared Quartz Heater)	2000	Non-focused	–

lighting. The scaling and orientation of the digital outcrop models were validated by placing three measuring sticks in each scene before image capture, aligned using a compass along the principal axes of the geographic coordinate system.

The low-resolution LiDAR model was processed with the iPhone's "3D Scanner App" (including simplification and HD texturing) and exported as a high-density point cloud in .ply format. The LiDAR overview models are automatically scaled based on distance measurements of the LiDAR and the iPhone's inertial measurement unit, the accuracy of which was verified with the measuring sticks placed in each scene. The resulting model has a point density of about 3.3 points/cm^2. Agisoft Metashape Professional v1.6.3 was used for the photogrammetric reconstruction of the DSLR images to obtain higher resolution models of each of

the three outcrops. The resulting point clouds (with a point density of 20–25 points/cm^2) were then georeferenced to the iPhone LiDAR model using the iterative closest point method implemented in CloudCompare (Girardeau-Montaut, 2020).

X-ray diffraction (XRD)

We determined XRD mineral abundances for 14 hand samples chipped off the mine face in outcrop Z1 after scanning. These hand specimens were manually located within about 5 cm by comparing images of the sampling locations and the dense 3D point cloud (see the "Geometric data" section). We chose XRD because it is a standard method that provides fast and reliable quantitative information on the type and concentration of minerals, including zinnwaldite and clays (Moore & Reynolds, 1997).

The samples were first scanned with the laboratory SiSuROCK scanner (see the "Drillcore scanner" section) to provide a hyperspectral characterisation before being crushed to a grain size < 400 μm using a steel mortar. They were then wet-milled with ethanol in a McCrone mill (Retsch) to a grain size < 10 μm, dried overnight, homogenised and filled into sample holders employing the backloading technique (to minimise orientation effects). A PANalytical Empyrean diffractometer, equipped with a Co-tube (operated at 35 kV, 35 mA), Fe-filter and a PIXcel3D Medipix 1×1 area detector, was then used to collect XRD spectra. The irradiated area was kept constant at 15×12 mm using a variable divergence slit. The measured 2-theta range was 5–80° with an overall measurement time of 153 min. We evaluated the obtained data via the Rietveld method using the BGMN/Profex bundle V5.1 (Doebelin & Kleeberg, 2015).

Hyperspectral data acquisition

We acquired hyperspectral data from three adjacent outcrops in the Zinnwald underground mine (Figure 1D). Based on the outcomes of the camera and light tests in the dark lab (see the fourth section) we chose the SPECIM Aisa Fenix 1K for the acquisition and a light set-up which included three 500 W halogen floodlights and one 1000 W halogen spotlight. We placed the floodlights at an even distance of about 2 m along the outcrop. The spotlight was mounted on a tripod, placed outside the scene at about 4 m from the outcrop and manually swivelled with the rotation of the hyperspectral camera to maximise the illumination of the area being scanned. We positioned the camera on a ledge 5.5–10 m from the first outcrop and 6–7 m from the second and third outcrops, respectively. Both the camera and the lights (in total about 2.8 kW) were powered by the mine's electricity grid. We acquired multiple scans with the same acquisition geometry for each outcrop, which we then averaged into a single hypercube during processing to increase the signal-to-noise ratio. Three scans were acquired for outcrops Z2 and Z3, respectively. Outcrop Z1 (dimensions: 13×1.5 m) is slightly larger than outcrops Z2 (10×1.7 m) and Z3 (7×1.5 m) and has a more complex geometry, so to cover it fully, we acquired nine scans in total, six of the left part and three of the right part.

Hyperspectral data processing

We have demonstrated that a proper 3D reference system is required to deliver accurate and useful HSI data (e.g., Jakob et al., 2017; Lorenz et al., 2018; Thiele et al., 2021). For the preprocessing of the data up to reflectance, see the "Data processing and co-registration" section. Before projecting the hyperspectral scans onto the photogrammetric point clouds using *hylite* (Thiele et al., 2021), we solved the position and orientation of the camera in every scene by manually collecting eight to 10 key point pairs to associate real-world coordinates (points in the dense photogrammetric point cloud) with image pixels. This alignment resulted in a residual of 1.7–2.3

pixels. Once a *hypercloud* was generated, we reduced artefacts introduced by the multi-light set-up by averaging multiple scenes and applying a normalisation based on the RGB information of the photogrammetric model. For visualisation, based on the known absorptions of the minerals of interest (e.g., the USGS Spectral Library, Cudahy et al., 2009; and the CSIRO Mineral Spectral Library, CSIRO, 2020), we combined the wavelengths 2200, 2250 and 2085 nm in a false-colour composite as an approximate measure for mica/clay-zinnwaldite-topaz (CZT) abundance (see the fourth section for details). We also built a false-colour composite Fe index comprised of several band ratios sensitive to Fe-bearing minerals, such as 600/570 nm for Fe^{3+}, $(920 + 1650\,nm)/(1035 + 1230\,nm)$ for Fe^{2+}, and $(2230 + 2290\,nm)/(2245 + 2260\,nm)$ for FeOH (Cudahy et al., 2009; Pontual et al., 2008). In addition, we visualised the data using a combination of bands based on a minimum noise fraction (MNF) transformation of the data for contrast enhancement (Green et al., 1988).

Mineral mapping and grade estimation

A three-step workflow was applied to derive modal mineralogy maps and associated grade estimates from the hyperspectral data. First, high-resolution Fenix images of each XRD sample (collected using the SiSuROCK scanner) were masked, averaged, hull corrected across the 700–2500 nm range and inverted to derive spectra containing absorbance peaks. The non-negative least squares optimisation described by Khodadadzadeh and Gloaguen (2019) was then applied to estimate pure mineral spectra from the measured mixed spectra and (XRD) mineral abundances, resulting in a pure end-member library. This method was used for three main reasons: (1) it is robust against overfitting; (2) it gives an interpretable end-member library; and (3) it has a (quasi-) physical basis to help mitigate the limited number of training data.

This end-member library was used to derive spectral abundances for each mineral on the underground rock face by unmixing the hyperspectral scans using the end-member library described above and the non-negative least squares method in *pysptools* (Therien, 2022). Spectral abundances were then extracted at each of the sampling locations, and fit to the measured modal (weight %) mineralogy using a linear regression. As it is standard practice with compositional data (Aitchison, 1986), both the spectral abundances and XRD modal mineralogy measurements were transformed using an additive log-ratio before the regression, ensuring the resulting (back-transformed) modal mineralogy estimates sum to one. The entire processing workflow is included as a Jupyter Notebook (see Appendix S1).

Qualitative LIBS validation

LIBS is a type of atomic emission spectroscopy in which a rapidly pulsed laser beam is focused onto a sample to form a plasma containing the constituent elements. The emitted light is then analysed to detect and identify each element (Harmon & Senesi, 2021). LIBS is a versatile method that can be performed in the laboratory or *in-situ* with a portable device and can provide qualitative and quantitative analyses of most elements on the periodic table. It is an ideal technique to measure light elements such as Li during fieldwork (Fabre et al., 2022; Harmon et al., 2005; Wise et al., 2022).

To validate the mineral maps produced from the hyperspectral SWIR data, we selected 11 locations from outcrop Z1 (Figure 1D) to measure with a SciAps Z-300 portable LIBS device. These locations contained varying amounts of mapped zinnwaldite as suggested by field observations and the hyperspectral data, ranging from 0 to >30 wt%. Measurements were taken in representative homogeneous circular areas from 5 to 16 cm in diameter, depending on accessibility, totalling 10–20 measurements per location, which we then averaged to estimate the Li content. Furthermore, a 100 cm straight profile was selected that stretches

diagonally over multiple lithologies. Along this profile, we collected five LIBS measurements every 10 cm, which were then averaged.

RESULTS

Outcrop sample characteristics

The mineralogical composition of the samples taken from outcrop Z1 of the Zinnwald mine (Figure 1E), as determined by XRD analysis, is 50–85 wt% quartz, 6–33 wt% zinnwaldite, < 31 wt% muscovite/illite, < 15 wt% topaz, < 10 wt% K-feldspar, < 10 wt% kaolinite and < 3 wt% fluorite (Figure 3a). In other parts of the Zinnwald/
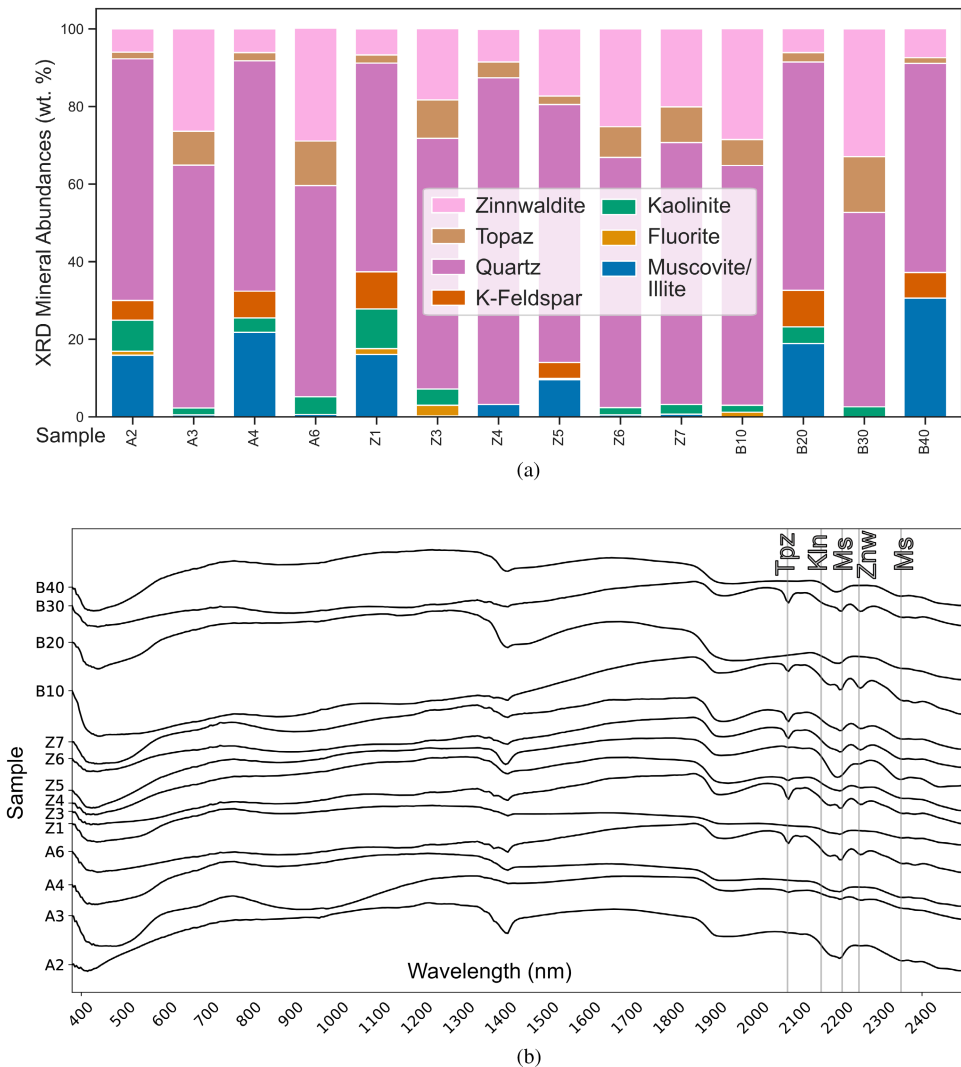

FIGURE 3 (a) X-ray diffraction mineralogical data; and (b) spectral characteristics (average spectra) of samples from the Z1 outcrop used for mineral mapping and grade estimation. Grey lines mark the main absorption features. Mineral abbreviation in (a) after Whitney and Evans (2010).

Cínovec deposit, albite may occur as another major mineral phase, but this was not observed here. Hence, in the VNIR and SWIR, the only spectrally active minerals are muscovite, zinnwaldite, kaolinite and topaz, the absorption features of which show no significant overlap (Figure 3b). Thus, the main lithologies in Zinnwald are spectrally very well-defined and (theoretically) clearly distinguishable.

Evaluation of light sources

A comparison of incandescent light sources (Figure 4a) shows that all the halogen lights provide continuous illumination over the entire spectral range of interest, with the highest at-sensor radiance in the upper VNIR range, a sharp drop-off into the lower VNIR range, and a more gradual drop-off into the SWIR range
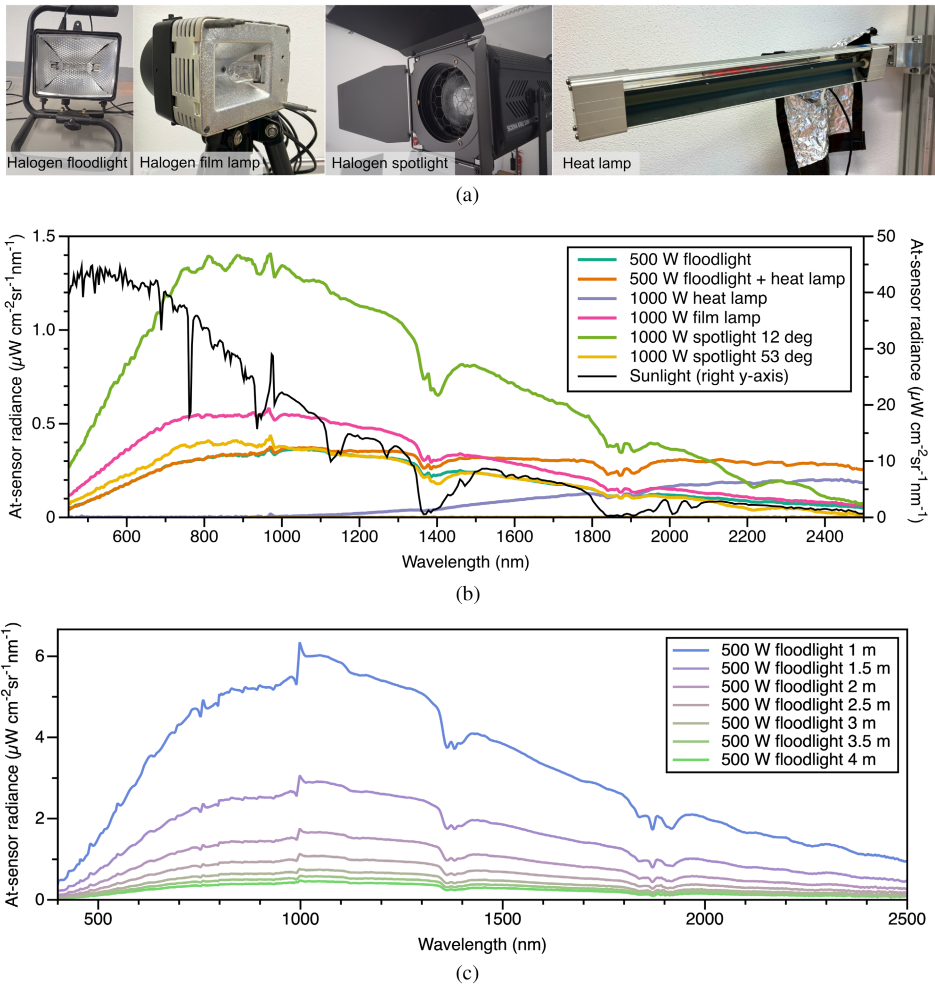

FIGURE 4 Results of the light experiments in the dark lab: (a) the different lights tested; (b) a spectral comparison of different light sources; and (c) the effect of distance on the spectral radiance of a halogen light source. Spectra are the measured at-sensor radiance after reflecting off a white panel. For (b), a common distance of 2.5 m between light source and target was chosen, approximately matching the distance used in the camera tests and in the underground mine. Absorptions at 1400 and 1900 nm are due to atmospheric water.

(Figure 4b). Whereas the spectral signature of the halogen lights is very similar, the absolute at-sensor spectral radiance of the halogen lights in our set-up depends both on the power of the light bulbs (compare the 500 W floodlight versus the 1000 W film lamp in Figure 4b), the field of view (FOV) of the light (compare the two FOV settings of the spotlight in Figure 4b), and the distance (Figure 4c). Following Equation (1), irradiance decreases with the square of the distance and FOV. Hence, light sources should be placed as close as possible to the outcrop and focused as much as the acquisition geometry allows. However, even at a 2.5 m distance, the mean irradiance of the most powerful and focused halogen light tested in this set-up (spotlight with 12° FOV) is about 20 times lower than in outdoor scenes lit by full sunlight (Figure 4b), so ideally, the target is illuminated with multiple lights. In addition, sensor exposure needs to be maximised and techniques such as data averaging applied to increase the signal-to-noise ratio. A combination of halogen and heat lamps would provide a more optimal spectral coverage (Figure 4b), but the heat poses a safety risk, and the heat lamps consume significantly more power than the halogen lamps.

$$\text{Irradiance} = \text{power} / \left(\pi^* \left(\text{distance}^* \tan \left(\text{FOV}/2 \right) \right)^2 \right) \text{(assuming circular spot).} \tag{1}$$

Sensor performance with underground settings

Both the false-colour composite images (Figure 5a) and the corresponding spectra (Figure 5b) reveal that all the hyperspectral sensors tested in the underground lab can successfully identify the main SWIR absorptions of the Zinnwald sample material. The Fenix 1K and Mjølnir have significantly more pixels than the Fenix (1024 and 640 versus 384 pixels) (Table 1), so they achieve higher spatial resolution than the Fenix for a given viewing distance but are slightly unfocused due to a target distance below the recommended minimum focusing distance of the camera (Table 1). However, as demonstrated by the similarity of the Fenix 1K and Mjølnir spectra (Figure 5b) to those of the SisuRock reference, the slight blurring of the image does not significantly degrade the spectral quality. The Fenix 1K achieved the best SNR, followed by Fenix and Mjølnir.

Influence of water

Moisture on rock surfaces, as revealed by qualitative tests in the underground laboratory, results in up to 40–50% reduction of the overall reflectance (Figure 6a), which can be explained by diffuse scattering and internal reflection (e.g., Lekner & Dorf, 1988). Water absorption features (at about 1400 and 1900 nm) deepen and broaden significantly to the point where they would potentially interfere with the absorption feature of topaz at 2085 nm. Mineral-related absorption features in the SWIR range extracted using minimum wavelength mapping (Figure 6b–d) broaden and decrease in depth with increasing moisture level. The broadening is particularly pronounced for smaller features, including the zinnwaldite absorption at 2250 nm. Isolated features, such as the topaz absorption at 2085 nm and large features such as the AlOH absorption at 2200 nm are not as pronounced under wet conditions but are still well-defined.

Underground mapping

The CZT abundance (Figure 7a), Fe ratio (Figure 7b) and MNF (Figure 7c) false-colour maps of outcrop Z1 indicate that the underground hyperspectral acquisitions achieved an excellent spectral quality, comparable with the data obtained in the laboratory tests. Because the distance between the sensor and the outcrop was below the recommended focusing distance of the camera, the images are slightly out of focus. Still, the resolution of Fenix 1K is large enough that principal spatial and spectral features are preserved. The
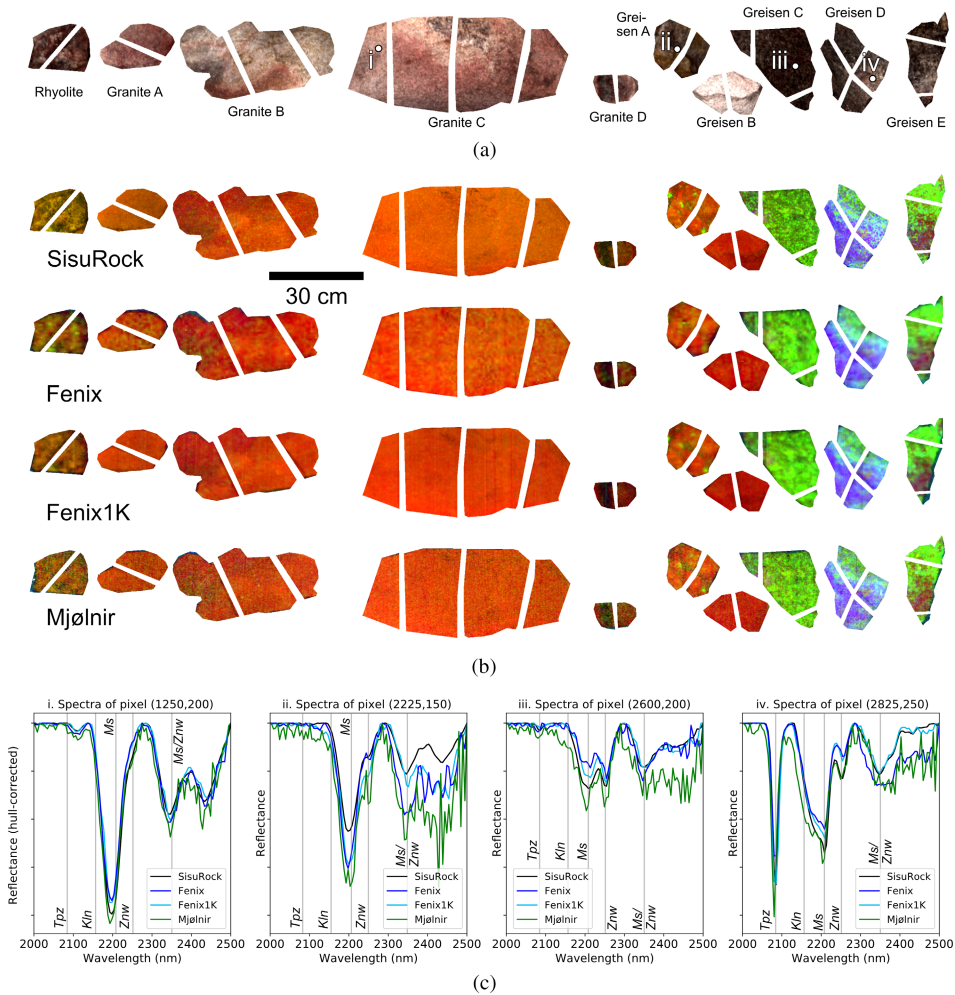
FIGURE 5 Comparison of hyperspectral sensors: (a) RGB image of the hand samples, masked to exclude the metal wire holding the samples in place; and (b) false colour combinations corresponding to absorbance (1 – hull-corrected reflectance) at wavelengths 2200 nm (red), 2250 nm (green) and 2085 nm (blue), which approximately relate to clay/mica, zinnwaldite and topaz, respectively. These, along with single pixel (i–iv) spectral comparisons (c), suggest comparable results were achieved with each sensor, though with varying amounts of noise. Grey lines mark the main absorption features.

relevant absorption features identified in the sample scans (Figure 2b, c) are all present in the underground hyperspectral data (Figure 7d). They can be used to distinguish white mica/clays, topaz, zinnwaldite, and Fe oxide minerals, revealing significant spatial variation that is not apparent from visual inspection of the outcrop (Figure 1e).

We then applied the workflow described in the "Mineral mapping and grade estimation" section to derive modal mineralogy maps. The non-negative least squares optimisation (to estimate the pure mineral spectra from the measured, mixed spectra and mineral abundances) yielded a pure end-member library of quartz/feldspar, zinnwaldite, muscovite/illite, kaolinite and topaz (Figure 8). This library provides an opportunity for evaluating the performance of the algorithm. Most end-member spectra show all the expected absorptions known from library spectra, apart from quartz, which exhibits an absorbance peak at about 2200 nm (Figure 8), perhaps due to a transparency effect or the mineralogical association of quartz and mica.
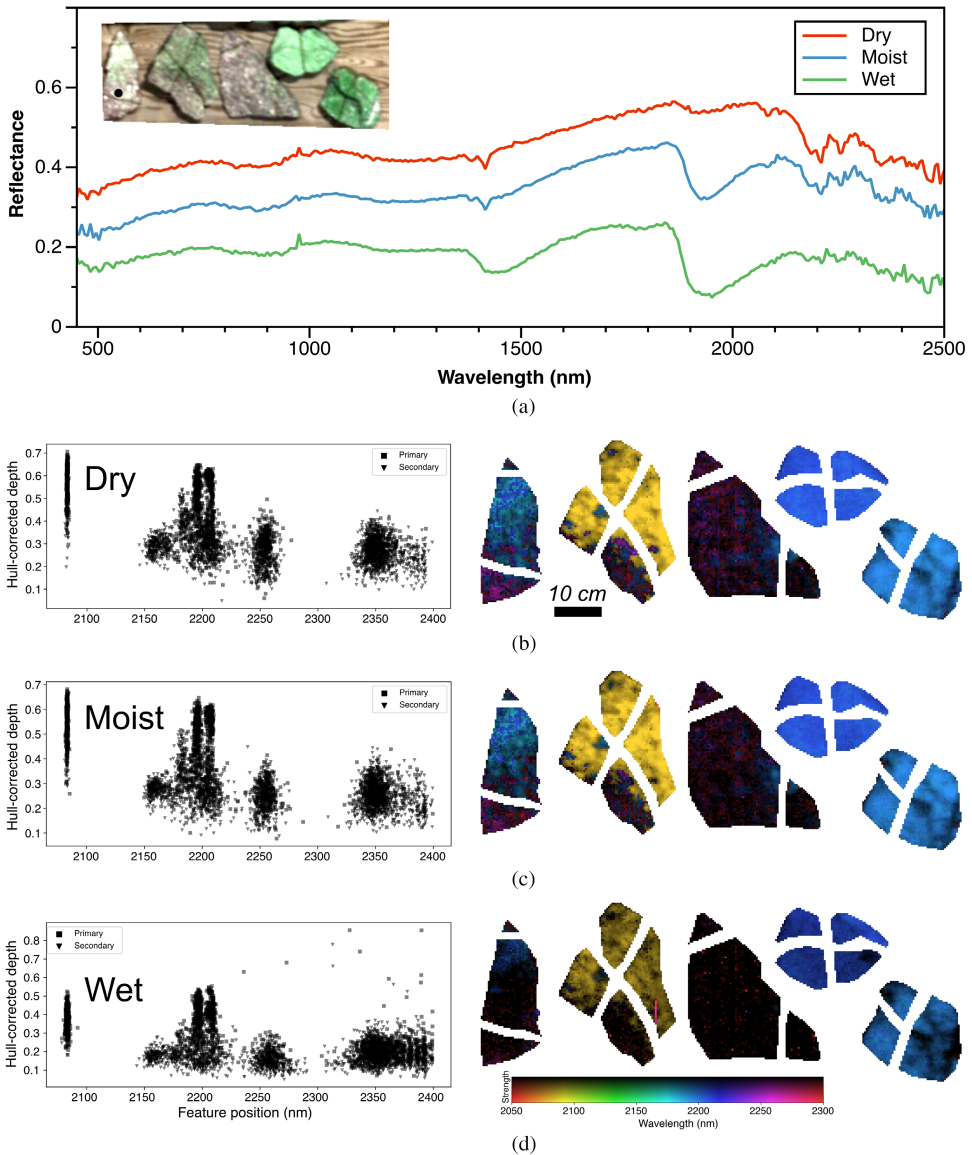
FIGURE 6 Influence of moisture on spectral reflectance: (a) example spectra; the inset shows the location of the sample point; and (b–d) minimum wavelength mapping results (fitting two Gaussian features on hull-corrected spectra in the 2030–2400 nm range) showing feature summary (left) and corresponding map, colour-coded by position=hue and depth=saturation (right).

After applying spectral unmixing and linear regression to convert spectral abundances to weight % modal mineralogy (cf. the "Mineral mapping and grade estimation" section), we derived a set of mineral maps (Figure 9) that appear geologically plausible and in line with field observations. The wave-like contact between a more and less greisenised lithologic unit (Qtz-Znw-Tpz greisen versus greisenised albite granite) (Figure 1e) is clearly defined (Figure 9b, d, e), as well as other key features noted in the field (haematite alteration zone, a quartz/muscovite vein with associated clay gauge and a zinnwaldite veinlet (Figure 1e). Numerically, the linear regression achieved an average R^2 score of 0.44. This relatively poor performance is dominantly due to an (unsurprisingly) poor prediction of quartz and feldspar ($R^2 = 0.07$) and the poor

Ternary image showing absorbance at 2200 (R), 2250 (G) and 2085 (B) nm, interpreted to correspond to mica/clay (R), zinnwaldite (G) and topaz (B).

(a)
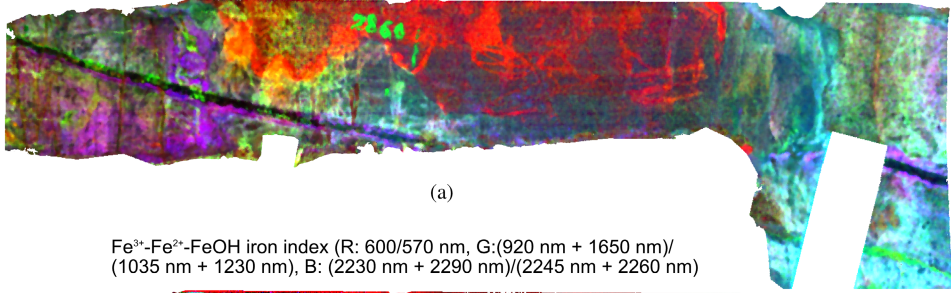
Fe³⁺-Fe²⁺-FeOH iron index (R: 600/570 nm, G:(920 nm + 1650 nm)/ (1035 nm + 1230 nm), B: (2230 nm + 2290 nm)/(2245 nm + 2260 nm)

(b)
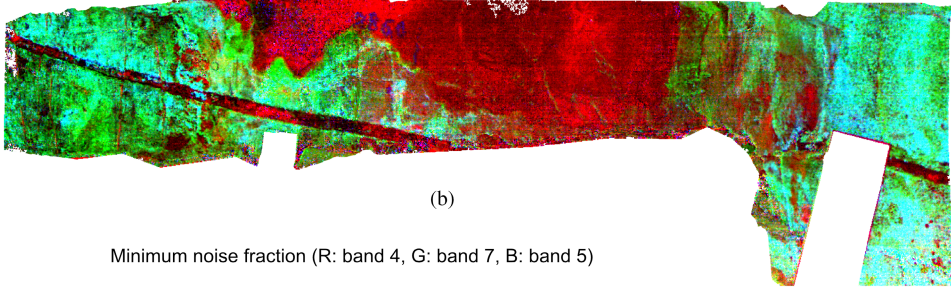
Minimum noise fraction (R: band 4, G: band 7, B: band 5)
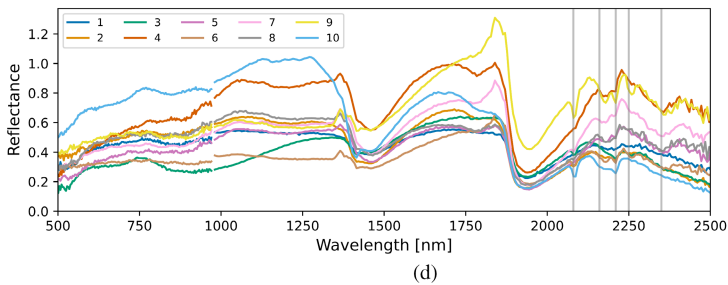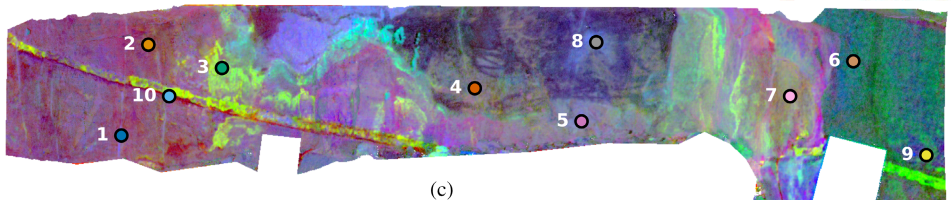
(c)

(d)

FIGURE 7 Hyperspectral data for outcrop Z1 in the Zinnwald mine: (a) mica/clay-zinnwaldite-topaz (CZT) abundance; (b) false-colour composite Fe index; (c) minimum noise fraction (MNF) image (bands R=4, G=7, B=5) to show spectral variability; and (d) representative image spectra. Grey lines highlight the positions of main mineral absorptions associated with topaz, kaolinite, mica/clay and zinnwaldite. Two bands around the sensor shift at 980 nm were masked before computing the MNF. For a 3D rendering of these maps, see https://tinyurl.com/Zinnwald.

prediction of kaolinite (0.169). The predictions of zinnwaldite ($R^2 = 0.61$), muscovite/illite ($R^2 = 0.65$) and topaz ($R^2 = 0.71$) are very good (Figure 9g).

Assuming zinnwaldite contains on average 1.7 wt% Li, and given it is the only Li-bearing mineral in this deposit (Neßler, 2016), the zinnwaldite abundance can be scaled to directly estimate Li grade (Figure 10), which accordingly ranges between 0.15% and 0.7% in outcrop Z1. The *in-situ* validation in this outcrop with a handheld LIBS instrument reveals a good qualitative agreement between the Li abundance estimated from the hyperspectral data and the relative Li content measured by LIBS (Figure 10).
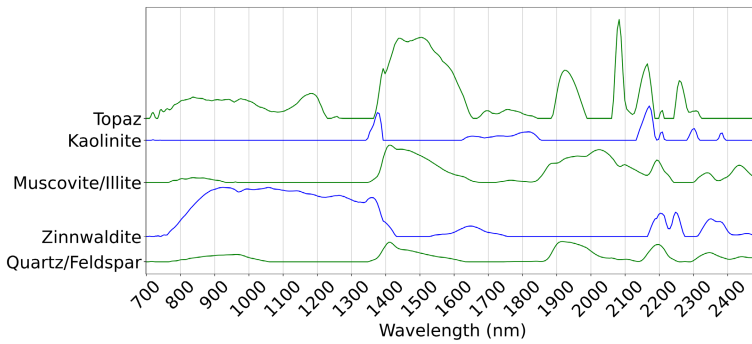
FIGURE 8 Pure end-member absorbance (1 – hull-corrected reflectance) spectra estimated using spectral measurements of the X-ray diffraction (XRD) samples and associated modal mineralogy. The absorption peaks of topaz, kaolinite and zinnwaldite generally match their expected positions. Quartz and muscovite/illite show mixed spectra, possibly as the large quartz grains are transparent in these wavelengths (i.e., they may inherit spectra from the surrounding minerals).

DISCUSSION

Limitations and recommendations

Our evaluation of different hyperspectral sensors suggests that all are appropriate for underground mapping of mineral assemblages found at the Zinnwald Li deposit. The signal-to-noise ratio is largest for the Fenix 1K, followed by Fenix and then Mjølnir, which reflects the size and price of the various sensors. Still, all tested instruments can detect the relevant mineral absorption features (Figure 5). Focus at short range is an issue for the Fenix 1K and Mjølnir, but could possibly be fixed with special fore-optics. The Fenix 1K also has high enough spatial resolution that some focal blur is tolerable. The ability to manually adjust the focus of the Fenix means it can be placed closer to the outcrop, though accurately setting focus in dark conditions may be difficult.

A comparison of the different lights tested indicates that tungsten spotlights are sufficient for underground HSI, although with rapidly decreasing power in the upper SWIR. Our experiments show that the combination of a tungsten halogen light with a heat lamp can achieve a better spread of power across the VNIR–SWIR wavelengths, so this can be considered for the future development of a broad-band light source. For the underground acquisitions, we used multiple light sources to illuminate the target from different angles. Although this set-up allowed us to illuminate a larger outcrop and minimise shadows, it creates an uneven, complex lighting scenario which is difficult to model and correct due to overlapping light cones, multi-directional shadowing and adjacency effects. We applied a correction of the hyperspectral data based on the (calibrated) RGB colour of the independently acquired photogrammetric point cloud, yet some illumination artefacts (e.g., large-scale gradients in the SWIR) remain, which may, to some degree, influence the mineral mapping. To avoid these problems, we suggest that the target be illuminated from the camera position using only a single light source, ideally by focusing the halogen light on a narrow strip that moves across the target together with the camera in push-broom fashion. Multiple acquisition locations combined with maximum-based blending techniques could then be used to reduce the influence of shadows while correcting properly for the lighting set-up. Recent developments of active hyperspectral sensors, that is, supercontinuum lasers operating in the VNIR–SWIR range (e.g., NKT Photonics; Chen et al., 2018; Kaariainen et al., 2019) could also represent a future alternative but at a much higher price.

As indicated by our laboratory tests, surface water results in more pronounced water absorptions, lowering of absolute reflectance (Lekner & Dorf, 1988), and a weakening/broadening of mineral absorptions in the SWIR.
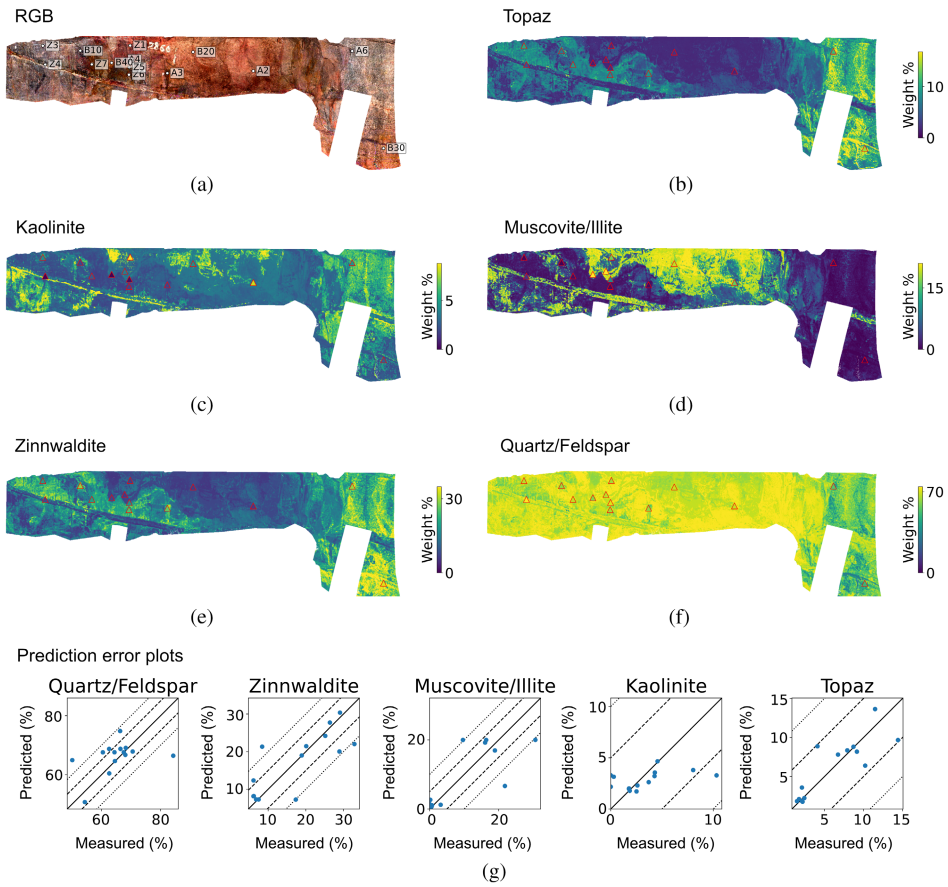
FIGURE 9 X-ray diffraction (XRD) sampling locations (a), derived modal mineralogy (b–f) estimated from the Z1 hyperspectral dataset (cf. the "Mineral mapping and grade estimation" section), and corresponding prediction error plots (g) showing 5% (dashed line) and 10% (dotted line) deviations from a one-to-one relationship. Red outlined triangles in mineral maps show the measured abundance of each XRD sample, demonstrating a generally close match. Key structures such as the quartz–mica vein, underlying clay gouge and contact between the zinnwaldite-greisen and altered albite granite (Figure 1e), are clearly defined. For a 3D view of these mineral maps, see https://tinyurl.com/Zinnwald.

FIGURE 10 Predicted Li grade for outcrop Z1 derived by multiplying the zinnwaldite abundance by its average Li content (1.7%). White outlined circles show relative (uncalibrated) Li values from the independent LIBS measurements. For the 3D version of this map, see https://tinyurl.com/Zinnwald.

Water films are also known to increase specular reflection, and the at-sensor radiance from specular reflection can exceed the radiance from the material of interest below the water surface (e.g., Kay et al., 2009). In addition, surface moisture has been observed to cause blurring, complicating the identification of mineral distribution (Schropp et al., 2013). Although surface moisture is present in the underground mine, our hyperspectral results suggest a limited impact on key features in the SWIR for this outcrop.

Added value for the mining industry

The hyperclouds generated from the hyperspectral and topographic survey of the Zinnwald outcrops allow us to quickly generate 3D feature maps based on dimensionality reduction algorithms such as PCA or MNF. These contrast-enhanced visualisations can help identify compositionally contrasting units, geological contacts and structures and guide sampling activities. Simple, unsupervised image processing algorithms such as band ratios and minimum wavelength analysis can directly map the relative distribution of Fe-bearing minerals, mica, clay, zinnwaldite and topaz in the outcrop. We extended these to obtain quantitative mineral abundance estimates across the outcrop using an innovative supervised mineral mapping approach that fuses a limited set of quantitative mineral abundance measurements with hyperspectral unmixing techniques. The workflow is novel in that it (1) yields mineral abundances (as opposed to classification maps in, e.g., Kurz et al., 2017; Lobo et al., 2021; Murphy et al., 2012); (2) uses XRD data (as opposed to SEM-MLA data in, e.g., Khodadadzadeh & Gloaguen, 2019); and (3) applies this approach at outcrop scale (as opposed to drill core scale in, e.g., De La Rosa et al., 2021; Khodadadzadeh & Gloaguen, 2019). This workflow enabled us to map the absolute abundance of infrared active minerals and, by inference, of Li, based on the known average Li content for zinnwaldite at the Zinnwald/Cínovec deposit. Limitations of these mineral maps include (1) the equal treatment of mineral abundance estimations from surface (HSI) and volume-based (XRD) methods; (2) an assumed linear relationship for the conversion from spectral to mineral abundance (linear mixing); and (3) possible influences of surface alteration, water and illumination artefacts. However, they reproduce a meaningful and validated mineral distribution highlighting key elements of the observed geology. The resulting hyperclouds map the 3D spatial distribution of mineral (or elemental) content on the surface of the three adjacent outcrops at high resolution (about 5 cm pixel size). Although beyond the scope of this paper, these could be used as inputs for 3D interpolation algorithms that extend these maps beyond the available exposures to help in, for example, resource modelling and mine planning.

Like many other industries, the extractive sector is in the midst of a data-driven revolution (Lööw et al., 2019; Nwaila et al., 2022). Many mining companies, for example, BHP Billiton, Rio Tinto and LKAB, are increasingly applying digital solutions to automate mines, including advanced sensor technology in the mining phase. The implementation of continuous hypercloud-based data analytics from successive underground mine drive faces would have breakthrough benefits for applications along the entire value chain of underground mining planning and production, for example, for (1) monitoring ore grade and volume and better separating ore from gangue during loading operations; (2) identifying and estimating the abundance and 3D distribution of minerals that adversely affect ore mineral recovery; (3) predictive mapping of discontinuities and of minerals that have a negative impact on mine stability to support structural and geotechnical mining planning; and (4) mapping of ore minerals or alteration mineralogies that are beneficial for determining vectors to ore bodies, updating existing 3D resource models or supporting the control of autonomous mining systems. Installing hyperspectral sensors (and illumination units) on (driverless, electric) mining trucks as part of a digital mining transformation will require further work on broadband lighting solutions and real-time processing workflows for fusing underground LiDAR or SfM and hyperspectral data. Another topic of further research is the underground deployment of long-wave hyperspectral sensors for better mapping abilities of rock-forming minerals such as quartz and feldspars (e.g., Laukamp et al., 2021).

CONCLUSIONS

We have successfully acquired high-quality, radiometrically corrected underground hyperspectral imagery and derived geologically meaningful, validated 3D mineral maps. This study demonstrates the feasibility of the hyperspectral mapping approach of large, complex outcrops in real underground mine conditions, that is, with poor lighting, rugged topography, moisture, and limited accessibility. Furthermore, by deriving quantitative maps of the abundance of Li-bearing ore minerals, we show that HSI can remotely map Li abundance to facilitate, for example, grade-control activities. We conclude that while the mining industry has not widely adopted (underground) hyperspectral face mapping, it is technically feasible and brings many advantages (e.g., objectivity, reproducibility, safety).

DATA AVAILABILITY STATEMENT

The raw data are available from the first author upon reasonable request. The interpreted data, that is, false colour visualisations and mineral maps, are available as point clouds in https://doi.org/10.14278/rodare.2078 (Kirsch et al., 2023) under Creative Commons Attribution 4.0 International licence. These point clouds can be visualised in 3D at https://tinyurl.com/Zinnwald. The Jupyter notebook that was used to create the mineral maps is included in Appendix S1.

ORCID

Moritz Kirsch https://orcid.org/0000-0003-1512-5511
Ayoub Fatihi https://orcid.org/0000-0001-8572-6553

REFERENCES

Aitchison, J. (1986) *The statistical analysis of compositional data*. London: Chapman and Hall. Available from: https://doi.org/10.1007/978-94-009-4109-0

Azevedo, M., Baczyńska, M., Hoffman, K. & Krauze, A. (2022) *Lithium mining: how new production technologies could fuel the global EV revolution*. New York, USA: McKinsey & Company. Available from: https://www.mckinsey.com/industries/metals-and-mining/our-insights/lithium-mining-how-new-production-technologies-could-fuel-the-global-ev-revolution [Accessed: 2nd January 2023].

Booysen, R., Lorenz, S., Thiele, S.T., Fuchsloch, W.C., Marais, T., Nex, P.A.M. et al. (2022) Accurate hyperspectral imaging of mineralised outcrops: an example from lithium-bearing pegmatites at Uis, Namibia. *Remote Sensing of Environment*, 269, 112790. Available from: https://doi.org/10.1016/j.rse.2021.112790

Chen, Y., Jiang, C., Hyyppa, J., Qiu, S., Wang, Z., Tian, M. et al. (2018) Feasibility study of ore classification using active hyperspectral LiDAR. *IEEE Geoscience and Remote Sensing Letters*, 15, 1785–1789. Available from: https://doi.org/10.1109/lgrs.2018.2854358

CSIRO. (2020) *CSIRO mineral spectral libraries*. Australia: Commonwealth Scientific and Industrial Research Organisation. Available from: https://mineralspectrallibraries.csiro.au/home [Accessed: 6th June 2023].

Cudahy, T.J., Jones, M. & Thomas, M. (2009) *Next generation mineral mapping: Queensland airborne HyMap and satellite ASTER surveys 2006–2008*. https://doi.org/10.13140/RG.2.1.2828.1844

De La Rosa, R., Khodadadzadeh, M., Tusa, L., Kirsch, M., Gisbert, G., Tornos, F. et al. (2021) Mineral quantification at deposit scale using drill-core hyperspectral data: a case study in the Iberian Pyrite Belt. *Ore Geology Reviews*, 139, 104514. Available from: https://doi.org/10.1016/j.oregeorev.2021.104514

Dittrich, T., Helbig, M., Kühn, K., Bock, W.-D. & Müller, A. (2020) The Zinnwald Lithium Project: transferring legacy exploration data into new mineral resources. *European Geologist Journal*, 49, 12–18. Available from: https://doi.org/10.5281/zenodo.3938862

Doebelin, N. & Kleeberg, R. (2015) Profex: a graphical user interface for the Rietveld refinement program BGMN. *Journal of Applied Crystallography*, 48(5), 1573–1580. Available from: https://doi.org/10.1107/S1600576715014685

Elvidge, C.D., Keith, D.M., Tuttle, B.T. & Baugh, K.E. (2010) Spectral identification of lighting type and character. *Sensors*, 10, 3961–3988. Available from: https://doi.org/10.3390/s100403961

European Commission. (2020) *Critical raw materials resilience: charting a path towards greater security and sustainability* (Communication from the Commission to the European Parliament, the Council, the European Economic and Social Committee and the Committee of the Regions). Available from: https://ec.europa.eu/docsroom/documents/42849 [Accessed: 6th June 2023].

Fabre, C., Ourti, N.E., Ballouard, C., Mercadier, J. & Cauzid, J. (2022) Handheld LIBS analysis for in situ quantification of Li and detection of the trace elements (Be, Rb and Cs). *Journal of Geochemical Exploration*, 236, 106979. Available from: https://doi.org/10.1016/j.gexplo.2022.106979

Fraser, S., Whitbourn, L.B., Yang, K., Ramanaidou, E., Connor, P., Poropat, G. et al. (2006) Mineralogical face-mapping using hyperspectral scanning for mine mapping and control. *Proceedings of the Australasian Institute of Mining and Metallurgy Publication Series*. Darwin, Australia: Australasian Institute of Mining and Metallurgy. AusIMM, pp. 227–232.

GeoSN. (2013) *Topographische Karte 5248-SO Altenberg-Zinnwald-Georgenfeld* [Map]. Staatsbetrieb Geobasisinformation Und Vermessung Sachsen (GeoSN).

Ghamisi, P., Shahi, K.R., Duan, P., Rasti, B., Lorenz, S., Booysen, R. et al. (2021) The potential of machine learning for a more responsible sourcing of critical raw materials. *IEEE Journal of Selected Topics in Applied Earth Observations and Remote Sensing*, 14, 8971–8988. Available from: https://doi.org/10.1109/JSTARS.2021.3108049

Girardeau-Montaut, D. (2020) *CloudCompare*. [Computer software]. Available from: http://www.danielgm.net/cc [Accessed: 13th April 2022].

Green, A.A., Berman, M., Switzer, P. & Craig, M.D. (1988) A transformation for ordering multispectral data in terms of image quality with implications for noise removal. *IEEE Transactions on Geoscience and Remote Sensing*, 26(1), 65–74. Available from: https://doi.org/10.1109/36.3001

Guarnieri, P., Thiele, S.T., Baker, N., Sørensen, E.V., Kirsch, M., Lorenz, S. et al. (2022) Unravelling the deformation of Paleoproterozoic marbles and Zn-Pb ore bodies by combining 3D-photogeology and hyperspectral data (Black Angel Mine, Central West Greenland). *Minerals*, 12(7), 800. Available from: https://doi.org/10.3390/min12070800

Harmon, R.S., De Lucia, F.C., Miziolek, A.W., McNesby, K.L., Walters, R.A. & French, P.D. (2005) Laser-induced breakdown spectroscopy (LIBS) – an emerging field-portable sensor technology for real-time, *in-situ* geochemical and environmental analysis. *Geochemistry: Exploration, Environment, Analysis*, 5(1), 21–28. Available from: https://doi.org/10.1144/1467-7873/03-059

Harmon, R.S. & Senesi, G.S. (2021) Laser-induced breakdown spectroscopy – a geochemical tool for the 21st century. *Applied Geochemistry*, 128, 104929. Available from: https://doi.org/10.1016/j.apgeochem.2021.104929

Hunt, G.R. (1977) Near-infrared (1.3–2.4) μm spectra of alteration minerals-potential for use in remote sensing. *Geophysics*, 44, 1974–1986. Available from: https://doi.org/10.1190/1.1440951

Jakob, S., Zimmermann, R. & Gloaguen, R. (2017) The need for accurate geometric and radiometric corrections of drone-borne hyperspectral data for mineral exploration: MEPHySTo—a toolbox for pre-processing drone-borne hyperspectral data. *Remote Sensing*, 9(1), 88. Available from: https://doi.org/10.3390/rs9010088

Kaariainen, T., Jaanson, P., Vaigu, A., Mannila, R. & Manninen, A. (2019) Active hyperspectral sensor based on MEMS Fabry-Perot interferometer. *Sensors*, 19, 2192. Available from: https://doi.org/10.3390/s19092192

Kay, S., Hedley, J.D. & Lavender, S. (2009) Sun glint correction of high and low spatial resolution images of aquatic scenes: a review of methods for visible and near-infrared wavelengths. *Remote Sensing*, 1(4), 697–730. Available from: https://doi.org/10.3390/rs1040697

Khodadadzadeh, M. & Gloaguen, R. (2019) Upscaling high-resolution mineralogical analyses to estimate mineral abundances in drill Core hyperspectral data. *IGARSS IEEE International Geoscience and Remote Sensing Symposium*. https://doi.org/10.1109/IGARSS.2019.8898441

Kirsch, M., Lorenz, S., Zimmermann, R., Andreani, L., Tusa, L., Pospiech, S. et al. (2019) Hyperspectral outcrop models for palaeoseismic studies. *Photogrammetric Record*, 34(168), 385–407. Available from: https://doi.org/10.1111/phor.12300

Kirsch, M., Lorenz, S., Zimmermann, R., Tusa, L., Möckel, R., Hödl, P. et al. (2018) Integration of terrestrial and drone-borne hyperspectral and photogrammetric sensing methods for exploration mapping and mining monitoring. *Remote Sensing*, 10(9), 1366. Available from: https://doi.org/10.3390/rs10091366

Kirsch, M., Mavroudi, M., Thiele, S., Lorenz, S., Tusa, L., Booysen, R. et al. (2023) Data publication: underground hyperspectral outcrop scanning for automated mine-face mapping—the lithium deposit of Zinnwald/Cínovec [Data Set]. Rodare. https://doi.org/10.14278/rodare.2078

Kurz, T.H., Buckley, S.J. & Becker, J.K. (2017) *Hyperspectral imaging: a novel geological mapping technique for subsurface construction sites*. World Tunnel Congress 2017 – Surface challenges – Underground solutions, Bergen, Norway.

Kurz, T.H., Buckley, S.J., Howell, J.A. & Schneider, D. (2011) Integration of panoramic hyperspectral imaging with terrestrial lidar data. *Photogrammetric Record*, 26(134), 212–228. Available from: https://doi.org/10.1111/j.1477-9730.2011.00632.x

Laukamp, C., Rodger, A., Legras, M., Lampinen, H., Lau, I.C., Pejcic, B. et al. (2021) Mineral physicochemistry underlying feature-based extraction of mineral abundance and composition from shortwave, mid and thermal infrared reflectance spectra. *Minerals*, 11(4), 347. Available from: https://doi.org/10.3390/min11040347

Lekner, J. & Dorf, M.C. (1988) Why some things are darker when wet. *Applied Optics*, 27(7), 1278–1280. Available from: https://doi.org/10.1364/AO.27.001278

Lobo, A., Garcia, E., Barroso, G., Marti, D., Fernandez-Turiel, J.L. & Ibanez-Insa, J. (2021) Machine learning for mineral identification and ore estimation from hyperspectral imagery in tin-tungsten deposits: simulation under indoor conditions. *Remote Sensing*, 13(16), 3258. Available from: https://doi.org/10.3390/rs13163258

Lööw, J., Abrahamsson, L. & Johansson, J. (2019) Mining 4.0—the impact of new technology from a work place perspective. *Mining, Metallurgy & Exploration*, 36(4), 701–707. Available from: https://doi.org/10.1007/s42461-019-00104-9

Lorenz, S., Salehi, S., Kirsch, M., Zimmermann, R., Unger, G., Vest Sørensen, E. et al. (2018) Radiometric correction and 3D integration of long-range ground-based hyperspectral imagery for mineral exploration of vertical outcrops. *Remote Sensing*, 10(2), 176. Available from: https://doi.org/10.3390/rs10020176

Luetzenburg, G., Kroon, A. & Bjork, A.A. (2021) Evaluation of the apple iPhone 12 pro LiDAR for an application in geosciences. *Scientific Reports*, 11(1), 22221. Available from: https://doi.org/10.1038/s41598-021-01763-9

Martino, R., McCann, P., Ray, R.K. & van der Ende, O. (2021) *Trends in underground hard-rock mining for gold and base metals*. New York, USA: McKinsey & Company. Available from: https://www.mckinsey.com/industries/metals-and-mining/our-insights/digging-deeper-trends-in-underground-hard-rock-mining-for-gold-and-base-metals [Accessed: 17th August 2022].

Moore, D.M. & Reynolds, C.R., Jr. (1997) *X-ray diffraction and the identification and analysis of clay minerals*, 2nd edition. Oxford, New York: Oxford University Press.

Murphy, R.J. & Monteiro, S.T. (2013) Mapping the distribution of ferric iron minerals on a vertical mine face using derivative analysis of hyperspectral imagery (430–970 nm). *ISPRS Journal of Photogrammetry and Remote Sensing*, 75, 29–39.

Murphy, R.J., Monteiro, S.T. & Schneider, S. (2012) Evaluating classification techniques for mapping vertical geology using field-based hyperspectral sensors. *IEEE Transactions on Geoscience and Remote Sensing*, 50, 3066–3080. Available from: https://doi.org/10.1109/TGRS.2011.2178419

Murphy, R.J., Taylor, Z., Schneider, S. & Nieto, J. (2015) Mapping clay minerals in an open-pit mine using hyperspectral and LiDAR data. *European Journal of Remote Sensing*, 48(1), 511–526. Available from: https://doi.org/10.5721/eujrs20154829

Nassar, N.T., Lederer, G.W., Brainard, J.L., Padilla, A.J. & Lessard, J.D. (2022) Rock-to-metal ratio: a foundational metric for understanding mine wastes. *Environmental Science & Technology*, 56(10), 6710–6721. Available from: https://doi.org/10.1021/acs.est.1c07875

Neßler, J. (2016) *Geologischer Aufbau, Mineralogie, Geochemie und Geochronologie der Li-Sn-W-Greisenlagerstätte Zinnwald, Osterzgebirge, Deutschland*. [Unpublished doctoral dissertation]. Technische Universität Bergakademie Freiberg.

Nwaila, G.T., Frimmel, H.E., Zhang, S.E., Bourdeau, J.E., Tolmay, L.C.K., Durrheim, R.J. et al. (2022) The minerals industry in the era of digital transition: an energy-efficient and environmentally conscious approach. *Resources Policy*, 78, 102851. Available from: https://doi.org/10.1016/j.resourpol.2022.102851

Panagiotou, G.N. & Michalakopoulos, T.N. (2020) *Mine planning and equipment selection 2000*, 1st edition. Boca Raton, FL: CRC Press. Available from: https://doi.org/10.1201/9780203747124

Pontual, S., Merry, N. & Gamson, P. (2008) *Spectral interpretation field manual. GMEX spectral analysis guides for mineral exploration*, Vol. 1–3. Victoria, Australia: AusSpec Int. Ltd.

Rossi, P., Mancini, F., Dubbini, M., Mazzone, F. & Capra, A. (2017) Combining nadir and oblique UAV imagery to reconstruct quarry topography: methodology and feasibility analysis. *European Journal of Remote Sensing*, 50(1), 1–12. Available from: https://doi.org/10.1080/22797254.2017.1313097

Sahu, H.B., Prakash, N. & Jayanthu, S. (2015) Underground mining for meeting environmental concerns - a strategic approach for sustainable mining in future. *Global challenges, policy framework & sustainable development for mining of mineral and fossil energy resources (Gcpf2015)*, 11, pp. 232–241. Available from: https://doi.org/10.1016/j.proeps.2015.06.030

Schropp, C., Knapp, H. & Neubert, K. (2013) Potential of NIR hyperspectral imaging in the minerals industry. In: Beyerer, J., Puente León, F. & Längle, T. (Eds.) *OCM 2013 - optical characterization of materials*. Karlsruhe: KIT Scientific Publishing, pp. 215–225.

Stemprok, M., Holub, F.V. & Novak, J.K. (2003) Multiple magmatic pulses of the Eastern Volcano-Plutonic Complex, Krušné hory/Erzgebirge batholith, and their phosphorus contents. *Bulletin of Geosciences*, 78(3), 277–296.

Taylor, Z., Nieto, J. & Johnson, D. (2013) Automatic calibration of multi-modal sensor systems using a gradient orientation measure. *IEEE/RSJ International Conference on Intelligent Robots and Systems (IROS)*. Tokyo, Japan. https://doi.org/10.1109/IROS.2013.6696516

Therien, C. (2022, July 22) *Welcome to the PySptools documentation*. PySptools. Available from: https://pysptools.sourceforge.io/ [Accessed: 6th June 2023].

Thiele, S.T., Lorenz, S., Kirsch, M., Acosta, I.C.C., Tusa, L., Herrmann, E. et al. (2021) Multi-scale, multi-sensor data integration for automated 3-D geological mapping. *Ore Geology Reviews*, 136, 104252. Available from: https://doi.org/10.1016/j.oregeorev.2021.104252

Tischendorf, G. & Forster, H.J. (1990) Acid magmatism and related metallogenesis in the Erzgebirge. *Geological Journal*, 25(3–4), 443–454. Available from: https://doi.org/10.1002/gj.3350250326

Tomek, F., Opluštil, S., Svojtka, M., Špillar, V., Rapprich, V. & Míková, J. (2021) Altenberg–Teplice Caldera sourced Westphalian fall tuffs in the central and western Bohemian Carboniferous basins (eastern Variscan belt). *International Geology Review*, 64(4), 441–468. Available from: https://doi.org/10.1080/00206814.2020.1858357

Tong, X., Liu, X., Chen, P., Liu, S., Luan, K., Li, L. et al. (2015) Integration of UAV-based photogrammetry and terrestrial laser scanning for the three-dimensional mapping and monitoring of open-pit mine areas. *Remote Sensing*, 7(6), 6635–6662. Available from: https://doi.org/10.3390/rs70606635

Whitney, D.L. & Evans, B.W. (2010) Abbreviations for names of rock-forming minerals. *American Mineralogist*, 95(1), 185–187. Available from: https://doi.org/10.2138/am.2010.3371

Wise, M.A., Harmon, R.S., Curry, A., Jennings, M., Grimac, Z. & Khashchevskaya, D. (2022) Handheld LIBS for Li exploration: an example from the Carolina Tin-Spodumene Belt, USA. *Minerals*, 12(1), 77. Available from: https://doi.org/10.3390/min12010077

Yang, K., Whitbourn, L., Mason, P. & Huntington, J. (2013) Mapping the chemical composition of nickel laterites with reflectance spectroscopy at Koniambo, New Caledonia. *Economic Geology*, 108(6), 1285–1299. Available from: https://doi.org/10.2113/econgeo.108.6.1285

SUPPORTING INFORMATION

Additional supporting information can be found online in the Supporting Information section at the end of this article.

How to cite this article: Kirsch, M., Mavroudi, M., Thiele, S., Lorenz, S., Tusa, L., Booysen, R. et al. (2023) Underground hyperspectral outcrop scanning for automated mine-face mapping: The lithium deposit of Zinnwald/Cínovec. *The Photogrammetric Record*, 38, 408–429. Available from: https://doi.org/10.1111/phor.12457